Bioactive Materials 45 (2025) 388–400

Contents lists available at ScienceDirect

Bioactive Materials

journal homepage: www.keaipublishing.com/en/journals/bioactive-materials

Protocol for engineering bone organoids from mesenchymal stem cells

Jian Wang [a,b,c,d,e,f,1], Dongyang Zhou [d,f,1], Ruiyang Li [a,b,c,1], Shihao Sheng [a,b,c,1], Guangfeng Li [d,e,f,g], Yue Sun [d,e,f], Peng Wang [a,b,c], Yulin Mo [d,e,f], Han Liu [d,f], Xiao Chen [a,b,c,d,f], Zhen Geng [d,f], Qin Zhang [d,f], Yingying Jing [d,f,**], Long Bai [d,f,***], Ke Xu [d,f,****], Jiacan Su [a,b,c,d,f,*]

[a] Department of Orthopedics, Xinhua Hospital Affiliated to Shanghai Jiao Tong University School of Medicine, Shanghai, 200092, China
[b] Trauma Orthopedics Center, Xinhua Hospital Affiliated to Shanghai Jiao Tong University School of Medicine, Shanghai, 200092, China
[c] Institute of Musculoskeletal Injury and Translational Medicine of Organoids, Xinhua Hospital Affiliated to Shanghai Jiao Tong University School of Medicine, Shanghai, 200092, China
[d] Institute of Translational Medicine, Shanghai University, Shanghai, 200444, China
[e] School of Medicine, Shanghai University, Shanghai, 200444, China
[f] National Center for Translational Medicine SHU Branch, Shanghai University, Shanghai, 200444, China
[g] Department of Orthopedics, Shanghai Zhongye Hospital, Shanghai, 200941, China

ARTICLE INFO

Keywords:
Bone organoids
3D bioprinting
Bioink
Mineralization
Vascularization

ABSTRACT

Bone organoids are emerging as powerful tools for studying bone development and related diseases. However, the simplified design of current methods somewhat limits their application potential, as these methods produce single-tissue organoids that fail to replicate the bone microarchitecture or achieve effective mineralization. To address this issue, we propose a three-dimensional (3D) construction strategy for generating mineralized bone structures using bone marrow-derived mesenchymal stem cells (BMSCs). By mixing BMSCs with hydrogel to create a bone matrix-mimicking bioink and employing projection-based light-curing 3D printing technology, we constructed 3D-printed structures, which were then implanted subcutaneously into nude mice, away from the native bone microenvironment. Even without external stimulation, these implants spontaneously formed mineralized bone domains. With long-term culture, these structures gradually matured into fully differentiated bone tissue, completing both mineralization and vascularization. This *in vivo* bone organoid model offers a novel platform for studying bone development, exploring congenital diseases, testing drugs, and developing therapeutic applications.

1. Introduction

Bone diseases, including osteoporosis, osteoarthritis, and various bone tumors, represent a significant public health challenge worldwide, particularly with an aging population [1,2]. Current treatment strategies often fall short of expectations, mainly due to the complexity of bone tissue [3]. Bone tissue consists not only of bone cells but also involves intricate interactions among various cell types, such as osteoblasts, osteoclasts, and bone marrow stromal cells, regulated by multiple signaling pathways that govern bone formation, resorption, and repair [4,5]. Additionally, factors such as blood supply, neural regulation, and mechanical loading contribute to forming a dynamic and multifactorial microenvironment [6–8]. This complexity poses significant challenges for bone regeneration therapies, as current methods struggle to replicate this intricate physiological environment, limiting their efficacy [9]. Traditional therapeutic approaches, such as pharmacological

Peer review under responsibility of KeAi Communications Co., Ltd.
* Corresponding author. Department of Orthopedics, Xinhua Hospital Affiliated to Shanghai Jiao Tong University School of Medicine, Shanghai, 200092, China.
** Corresponding author. Institute of Translational Medicine, Shanghai University, Shanghai, 200444, China.
*** Corresponding author. Institute of Translational Medicine, Shanghai University, Shanghai, 200444, China
**** Corresponding author. Institute of Translational Medicine, Shanghai University, Shanghai, 200444, China.
E-mail addresses: jingy4172@shu.edu.cn (Y. Jing), bailong@shu.edu.cn (L. Bai), kexu@shu.edu.cn (K. Xu), jiacansu@shu.edu.cn (J. Su).
[1] These authors contributed equally to this work.

https://doi.org/10.1016/j.bioactmat.2024.11.017
Received 9 October 2024; Received in revised form 12 November 2024; Accepted 12 November 2024

interventions and surgical procedures, often fail to address the underlying pathophysiological processes effectively [10]. These conventional methods may not account for individual variations in disease mechanisms, making it challenging to achieve personalized and effective care for patients with diverse clinical presentations [11–13]. In this context, bone organoids, three-dimensional (3D) self-organized constructs derived from stem cells, offer a breakthrough by replicating bone tissue's architecture and function *in vitro* [14,15]. Unlike traditional models, bone organoids mimic the cellular diversity and spatial organization of human bone, providing a valuable tool for studying disease mechanisms, developing therapies, and enabling personalized medicine approaches [16–20].

The challenge lies in the overly simplified structure of existing bone organoid models, which typically generate single-tissue constructs lacking the necessary cues and interactions required for proper mineralization [21,22]. These models often omit essential biochemical and mechanical signals and the complex interactions between osteoblasts, osteoclasts, and stromal cells—critical components for bone formation and remodeling [23,24]. Moreover, they do not adequately replicate the vascularization, neural innervation, and the dynamic mechanical forces that are inherent to the *in vivo* bone environment [25–27]. Without these critical components, the models struggle to mimic the true regenerative capabilities of bone tissue, limiting their utility in both research and therapeutic applications [28]. To advance the field, more sophisticated organoid systems are needed, incorporating multiple cell types and simulating the biochemical and mechanical environments of bone tissue to better model bone development, disease, and regeneration [29]. This limitation not only hinders the study of bone-related diseases but also restricts the application of these organoids in drug testing and tissue engineering [15]. Thus, developing more complex bone organoid systems that can faithfully replicate the mineralization process observed *in vivo* is urgently needed [30].

To address this challenge, we have developed a novel method for constructing mineralization-capable bone organoids using bone marrow-derived mesenchymal stem cells (BMSCs) [31]. By utilizing advanced 3D printing technology and bone matrix-inspired bioink formulations, we have created a platform capable of generating bone organoids with enhanced mineralization potential (Fig. 1). This approach involves precisely combining BMSCs with hydrogels to form bioinks, which are then used in projection-based light-curing 3D

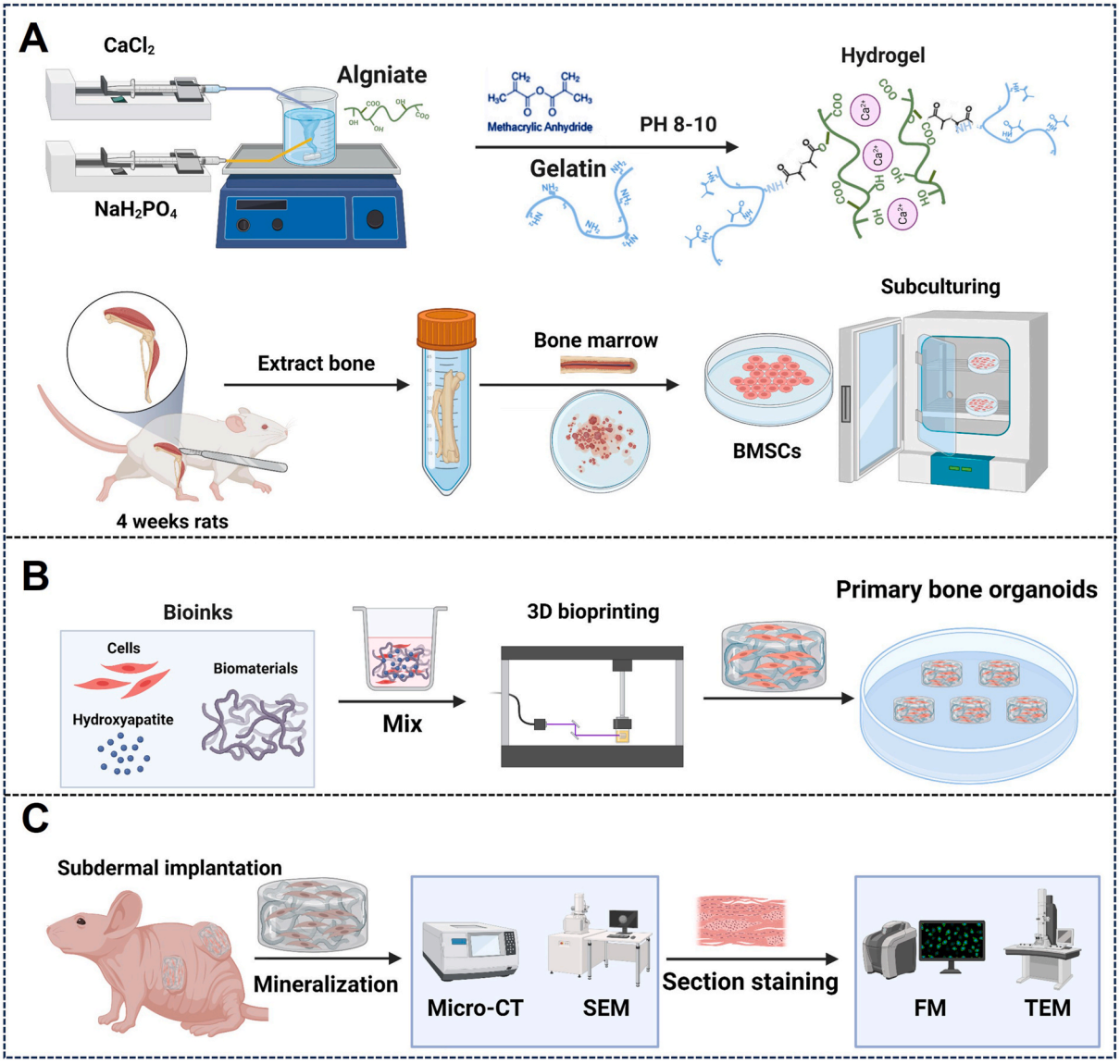

Fig. 1. Schematic overview of this protocol. (A) Preparation of bioink: hybrid hydroxyapatite hydrogels were synthesized, and rat BMSCs were isolated, extracted, and expanded *in vitro*. (B) 3D bioprinting of bone organoids. (C) *In vivo* cultivation and assessment of bone organoids.

printing to fabricate bone organoids [32]. After implanting these organoids into an *in vivo* model, we observed spontaneous mineralization and maturation of the bone structures, resulting in fully differentiated and vascularized bone tissue. This introduction lays the groundwork for exploring this innovative method, highlighting its potential to overcome the limitations of current bone organoid models and offering new opportunities for research and therapeutic applications in bone biology.

2. Development of bone organoid cultures

In earlier research by our group and others, protocols were developed to support the long-term growth of organoids derived from stem cells from a variety of tissues [31]. The initial advancements focused on the creation of intestinal organoids [33], which later expanded to include the development of organoid cultures specific to organs such as the lung, liver, and kidney [34–36]. Unique culture conditions were fine-tuned for each organoid type, with all requiring embedding and cultivation within extracellular matrix-based hydrogels [37]. Notably, specific culture protocols were designed to enable the sustained expansion of mesenchymal stem cells (MSCs) into bone organoids [14]. Under these culture conditions, MSCs are effectively induced to differentiate into osteoblasts and osteocytes by modulating key signaling pathways involved in bone development and remodeling, such as the wingless/integrated (Wnt), transforming growth factor-beta (TGF-β), and bone morphogenetic protein (BMP) pathways [38,39]. Although MSCs have long been used to model bone-like tissues, the direct expansion of mature bone cells in a 3D organoid system remained a challenge until recent breakthroughs. With the optimization of culture conditions, recent studies have demonstrated the feasibility of long-term expansion of BMSCs into bone organoids [40,41].

Traditional studies primarily focused on 2D culture methods for inducing osteogenic differentiation of MSCs. In contrast, our study aims to construct 3D bone organoids that can differentiate into a variety of bone-related cell types using an *in vivo* approach. Specifically, we developed a protocol that embeds BMSCs in a hybrid hydrogel enriched with hydroxyapatite and utilizes digital light processing (DLP) 3D bioprinting technology to fabricate scaffolds with bioinspired bone microstructures. The scaffolds were then implanted subcutaneously into nude mice to leverage the *in vivo* environment as a biological reactor, promoting differentiation into multiple bone-related cells, including osteoblasts, osteoclasts, chondrocytes, and adipocytes, instead of limiting differentiation to osteogenic lineages. This strategy enabled the formation of large-scale bone organoids capable of spontaneous mineralization and vascularization. Immunofluorescence analysis confirmed the presence of key bone markers, such as osteopontin (OPN) and osteocalcin (OCN), along with a diverse array of bone-associated cell types, demonstrating the effectiveness of our approach in replicating the complexity of bone tissue *in vivo*.

3. Applications of the methods and future possibilities

The establishment of bone organoid culture provides critical support for fundamental bone biology research [42]. Due to their long-term stability, bone organoids can model various bone diseases and be used to evaluate drug effects on bone tissue, particularly in studies related to bone regeneration, fracture healing, and metabolic bone diseases [43,44].

As an alternative to traditional bone transplantation, bone organoids can overcome challenges such as donor shortages, immune rejection, and surgical complications [45]. Through 3D bioprinting and 3D culture technologies, bone organoids can be precisely tailored to match the shape and structure of a patient's bone defects, enabling personalized treatments [46]. Especially in the repair of large bone defects, the combination of bone organoids with biomaterials and active cells can significantly enhance the functionality of the repaired tissue and accelerate healing [47]. Furthermore, bone organoids hold significant potential for drug screening applications. By establishing high-throughput screening platforms, they can simulate the *in vivo* microenvironment, reduce reliance on animal models, accelerate drug development, and lower costs [48]. Through genomics and proteomics, bone organoids can reveal drug mechanisms of action and identify potential therapeutic targets, supporting the development of personalized therapies [18]. In mechanistic studies, the 3D structure and complex cell interactions in bone organoids can help researchers gain deeper insights into bone development and pathological processes, revealing critical aspects of osteocyte behavior, matrix formation, and vascularization [49,50]. Bone organoids are also valuable for evaluating bone implants. By utilizing human-derived bone organoid models, researchers can more accurately simulate the human bone environment, provide more reliable preclinical data, and reduce the need for animal experiments. As technology continues to advance, the application prospects of bone organoids in precision medicine are becoming increasingly apparent [51]. By constructing patient-specific bone organoid models, it is possible to better simulate disease states, explore drug mechanisms in these models, and promote the development of personalized therapies [52]. In summary, bone organoids offer not only an innovative platform for basic research but also create new opportunities in clinical applications and drug development, contributing significantly to the progress of bone tissue engineering and regenerative medicine [53].

4. Experimental design

In the current protocol, we outline the experimental procedures for establishing bone organoids. In **Procedure 1**, we describe the isolation and expansion of BMSCs *in vitro*. To support BMSC proliferation and differentiation, we synthesized a matrix material composed of gelatin, alginate, and hydroxyapatite, which we cross-linked by introducing methacrylate (MA) groups for photocuring. This matrix, combined with BMSCs, forms a hybrid hydroxyapatite bioink used to construct 3D bone organoid systems. This section provides detailed guidance on the formulation of the matrix material and bioink, covering the steps for chemical synthesis as well as the specific procedures for establishing the cell culture system. In **Procedure 2**, we examine the construction process of bone organoids by first developing a porous model using 3D Max software, followed by fabricating the organoids with a DLP 3D printer. This section includes a detailed explanation of the steps involved and the key considerations for successfully constructing bone organoids. Finally, in **Procedure 3**, we implant bone organoids subcutaneously into nude mice and describe their *in vivo* development into bone tissue, independent of the native bone microenvironment. Multidimensional real-time evaluations of the bone organoids are conducted. Detailed experimental design considerations and step-by-step protocol guidelines are provided below.

4.1. Procedure 1: preparation of hydroxyapatite hybrid bioink

4.1.1. Synthesis of bioinspired bone matrix hydrogel

The bioinspired bone matrix hydrogel is designed to replicate the composition and properties of natural bone by incorporating organic collagen and inorganic hydroxyapatite, emulating the native extracellular matrix. Collagen provides elasticity and biocompatibility, hydroxyapatite offers structural strength and promotes mineralization. However, conventional methods that rely solely on mixing functional components often result in uneven distribution, with nano-sized hydroxyapatite tending to aggregation within the hydrogel. To overcome this limitation, we incorporated calcium chloride and disodium hydrogen phosphate during the incorporation of photocurable methacrylate groups, facilitating in-situ mineralization and ensuring uniform dispersion of the active components. This enhanced hydrogel structure more accurately mimics the natural bone matrix, providing an optimized environment for cell proliferation, differentiation, and mineralization.

a) In a 100 mL beaker, taking into account the thermosensitivity of gelatin during dissolution, 10 g of gelatin was added to 50 mL of deionized water and stirred on a heated magnetic stirrer at 300 rpm and 50 °C until a homogeneous 20 wt% solution without precipitation was formed.
b) In another 100 mL beaker, 0.5 g of sodium alginate was dissolved in 42 mL of deionized water. The beaker was covered with plastic film to prevent evaporation, and the solution was stirred at room temperature at 300 rpm using a magnetic stirrer for 4–6 h until the sodium alginate was fully dissolved.
c) Subsequently, 4 mL of 1 M $CaCl_2$ and 0.6 M NaH_2PO_4 solutions were gradually added at a rate of 50 μL/min using an intravenous micro-pump. The pH was adjusted to 8–10 with 3 M NaOH, and the solution was stirred at 500 rpm for 12 h on a magnetic stirrer.
d) Next, both solutions were preheated to 50 °C and stirred at 500 rpm on a magnetic stirrer for 2 h to ensure thorough mixing. Subsequently, 4 mL of methacrylic anhydride was gradually added at a rate of 0.5 mL/min using an intravenous micro-pump, while the pH was adjusted to 8–10 with 3 M NaOH. The reaction was carried out at 50 °C for 3 h. To terminate the reaction, 300 mL of deionized water preheated to 50 °C was added and stirred for 30 min.
e) To remove residual small molecules from the system, the mixture was cooled to 37 °C, placed in a dialysis bag with a 13,000-Da molecular weight cutoff, and dialyzed in a container filled with 10 L of deionized water for 7 days, with the water replaced twice daily.
f) The dialyzed solution was transferred into a 500 mL beaker and stirred at 300 rpm on a magnetic stirrer for 1 h to ensure uniform dispersion. The solution was then quickly distributed into 50 mL centrifuge tubes, each containing 45 mL of liquid to prevent rupture in liquid nitrogen. The tubes were placed in liquid nitrogen and frozen for 3 h. After freezing, the caps were removed, the tubes sealed with a porous membrane, and immediately placed in a freeze dryer. The freeze dryer was set to −80 °C with a vacuum pressure of 0 Mbar. The drying process continued for 1 week until all the liquid evaporated, resulting in solid hydrogel materials, which were sealed and stored to prevent moisture absorption.

4.1.2. Isolation, extraction, and culture of rat BMSCs

Stem cells serve as the foundation for organoid construction. BMSCs, with their self-renewal and multipotent differentiation capabilities, differentiate into the various cell types required for bone organoid formation. Therefore, in our bioink, we utilized rat BMSCs as seed cells and carried out the isolation, extraction, and culture of primary rat BMSCs.

a) Before isolating rat BMSCs, ensure all surgical instruments are sterilized and prepare a sterile working area. Euthanize the rat according to institutional ethical guidelines. The ethical approval number is provided in Procedure 3.
b) After euthanasia, place the rat in a supine position and disinfect the hind limbs with 70 % ethanol. Make an incision to expose the femur and tibia, carefully remove the surrounding muscle tissue without damaging the bones, and place the excised femur and tibia into cold, sterile PBS solution.
c) Under sterile conditions, cut off the ends of the bones to expose the marrow cavity. Flush the cavity with sterile PBS or DMEM using a syringe and collect the marrow into a 50 mL centrifuge tube. Continue flushing until the bones turn white, indicating complete marrow extraction. Gently pipette the solution to disperse cell clumps.
d) To maximize cell yield, add 0.1 % type I collagenase to the bone marrow suspension and incubate at 37 °C for 30 min with gentle shaking. After digestion, filter the solution through a 70 μm cell strainer to remove large debris and bone fragments.
e) Centrifuge the filtered suspension at 300×*g* for 5 min at room temperature. Discard the supernatant and resuspend the cell pellet in 10 mL DMEM containing 10 % fetal bovine serum (FBS) and 1 % penicillin-streptomycin (P/S).
f) Plate the cell suspension in a 100 mm culture dish and incubate at 37 °C in a 5 % CO_2 humidified incubator. After 24–48 h, wash away non-adherent cells with PBS, leaving the adherent BMSCs for further culture.
g) Replace the culture medium every 2–3 days. Once the cells reach 80–90 % confluency, detach them using 0.05 % trypsin-EDTA at 37 °C for 3–5 min. Collect the detached cells by centrifugation and resuspend them in fresh medium. The cells can be further expanded or cryopreserved for future use.

4.2. Procedure 2: construction of bone organoids

The construction of bone organoids involves 3D bioprinting using a bioink composed of BMSCs embedded in a hydrogel solution. The 3D model is designed with a cylindrical scaffold featuring square holes to facilitate material exchange. The printing process is carefully optimized to maintain precision and structural integrity. After printing, the bone organoids are rinsed and cultured in standard medium for several days before being transferred to an osteogenic induction medium supplemented with components that promote mineralization, collagen synthesis, and cell differentiation.

a) The 3D model was created using 3D Studio Max software (Autodesk, USA) and features a cylindrical structure with a diameter of 7 mm and a thickness of 2 mm. Inside, 21 square holes are evenly distributed in a grid pattern (Fig. 2B), facilitating material exchange between the interior and exterior of the scaffold.
b) Dissolve lithium phenyl-2,4,6-trimethylbenzoylphosphinate (LAP) in α-MEM medium containing serum and antibiotics to prepare a 0.25 wt% solution. Next, add the light absorber EFL-UVAW-001 to achieve a concentration of 0.05 wt% and mix thoroughly. Freeze-dry the hydrogel material prepared in Procedure 2, grind it into powder, and sterilize it under UV light for 1 h. Add the sterilized hydrogel powder to the prepared medium to formulate a 10 wt% hydrogel solution, and place it in a 37 °C water bath to maintain a constant temperature. Digest the extracted BMSCs, count the cells using a hemocytometer, and add them to the hydrogel solution to achieve a cell concentration of 1×10^6, thereby preparing bioink suitable for 3D bioprinting. All procedures must be performed under light-protected conditions.
c) During the 3D printing process, a DLP printer manufactured in China (EFL-BP-8601 Pro) was utilized to ensure high-resolution printing and stable performance. To achieve high-quality results, the printing parameters were meticulously optimized for the bioink, with specific settings to ensure stable material formation and structural integrity. The detailed parameters included a light intensity of 14 mW cm^{-2} and an exposure time of 12 s to ensure adequate curing of the material during printing. The number of base layers was set to 2, with a slightly longer exposure time of 14 s per base layer to provide sufficient strength for the foundational structure. The material's penetration depth was controlled at 50 μm to ensure precise detail in the print while preventing excessive penetration that could compromise structural stability. Throughout the printing process, the temperature of the platform and resin tank was maintained at 37 °C to preserve the bioink's flowability and operability, ensuring consistent performance without being affected by temperature fluctuations.
d) Gently place the printed bone organoids into sterile PBS solution at 37 °C and rinse three times. Then, transfer them into α-MEM medium containing 10 % serum and 1 % penicillin-streptomycin (P/S), and incubate for 3 days.
e) After 3 days, replace the osteogenic induction medium. The osteogenic induction medium is prepared based on DMEM, typically supplemented with 10 % fetal bovine serum (FBS) and 1 % penicillin-streptomycin (P/S). To promote osteogenic differentiation, 10 mM

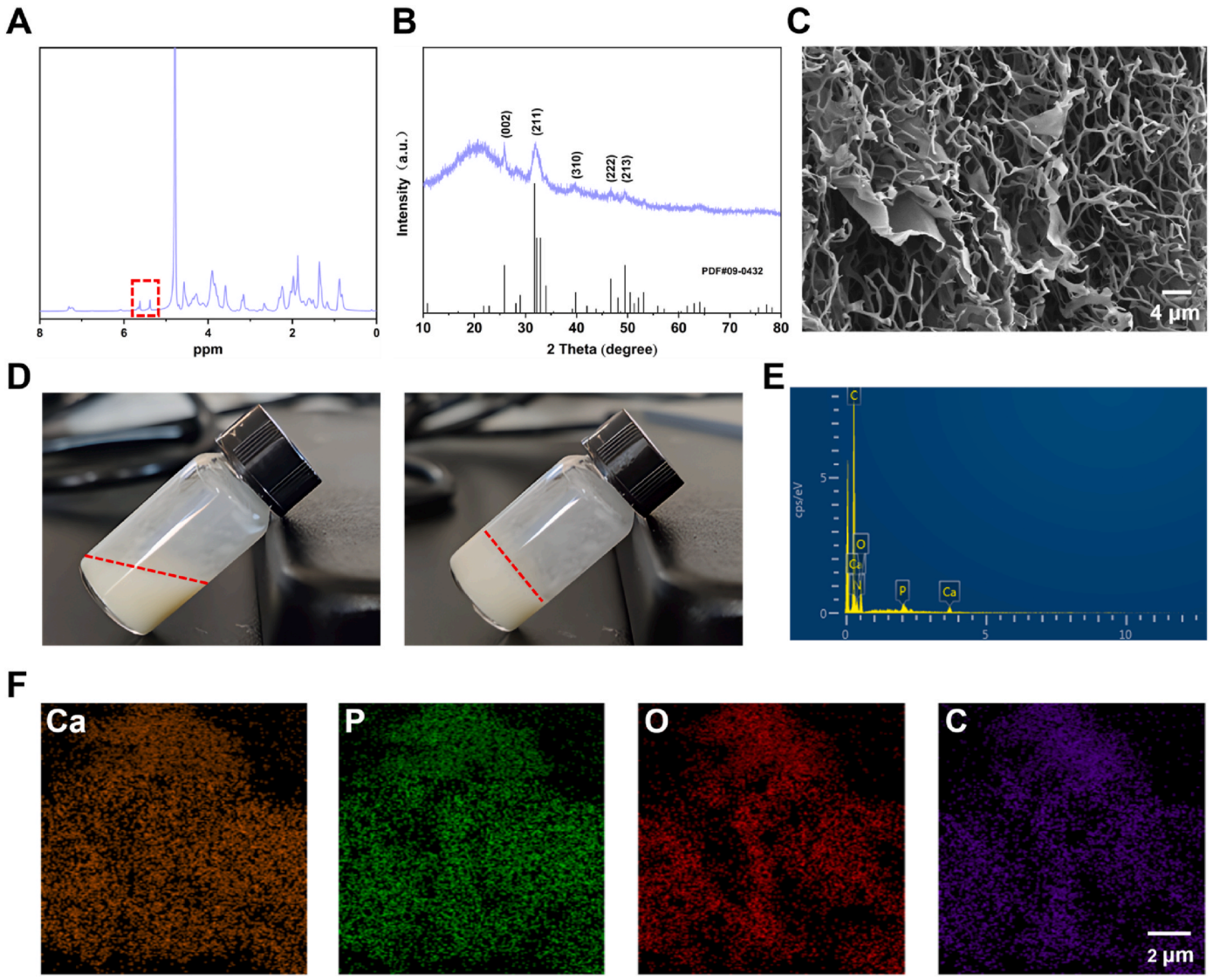

Fig. 2. Characterization of bone matrix-inspired hybrid hydroxyapatite bioink. (A) NMR spectroscopy of hybrid hydroxyapatite bioink. (B) XRD analysis of hybrid hydroxyapatite bioink. (C) SEM analysis of hybrid hydroxyapatite bioink. (D) Solution state of bioink before and after photopolymerization. (E) Elemental composition evaluation of bioink using EDS. (F) Elemental mapping of bioink.

β-glycerophosphate is added to enhance mineralization, 50 μg/mL ascorbic acid is included to stimulate collagen synthesis, and 100 nM dexamethasone is used to induce cell differentiation. After mixing all components thoroughly, the medium is sterilized by passing it through a 0.22 μm filter. The prepared osteogenic induction medium should be stored at 4 °C and used within two weeks to maintain its effectiveness.

4.3. *Procedure 3: subcutaneous in vivo culture in nude mice*

Eight-week-old female nude mice were obtained from Changzhou Cavens Experimental Animal Co., Ltd.

a) First, connect the isoflurane vaporizer and anesthesia machine to the oxygen supply, with the oxygen flow rate set to 0.5–1.5 L/min. Set the isoflurane concentration to 3–5% for induction anesthesia, during which the nude mice typically lose consciousness within 30 s to 1 min. Monitor the respiratory rate and response to assess the depth of anesthesia. Once anesthesia is achieved, adjust the isoflurane concentration to 1–3% to maintain anesthesia and use a face mask to continuously deliver the gas, ensuring effective anesthesia throughout the procedure. During the operation, regularly check the respiratory rate, heart rate, and pain reflex to ensure the appropriate depth of anesthesia.
b) A sterile scalpel is used to make an approximately 1 cm incision along the midline or lateral region of the dorsal skin of the nude mice. The incision should only penetrate the skin and subcutaneous tissue, avoiding damage to deeper structures. Sterile blunt forceps are then used to gently separate the subcutaneous tissue, creating sufficient space to accommodate the bone organoid. The prepared bone organoid is carefully implanted into the subcutaneous space using a spoon-like instrument, ensuring that the implant is stable and properly positioned. After implantation, the skin is precisely sutured with sterile surgical thread, typically using continuous or interrupted sutures, to ensure complete wound closure and reduce the risk of infection.
c) After the procedure, discontinue isoflurane administration and continue the oxygen supply for a few minutes to aid recovery. Finally, place the mice in a warm, sterile environment and monitor them until they fully recover.
d) Postoperatively, penicillin-streptomycin was chosen for antibiotic treatment to prevent infection. The recommended dosage is 10,000

U of penicillin and 10 mg of streptomycin per mouse per day, administered via intraperitoneal injection for 3–5 consecutive days to cover the high-risk period for postoperative infections.

e) During the *in vivo* culture period, the growth status of the nude mice was regularly monitored, and according to the experimental design, samples were collected at specific time points (e.g., 40 days) by extracting the implants for further analysis.

4.4. Characterization of bioink and identification of bone organoids

The characterization of bone organoids involves a comprehensive evaluation of their morphology, functionality, and biological properties. At the bioink level, nuclear magnetic resonance (NMR) spectroscopy is used to verify the grafting of photocurable groups, X-ray diffraction (XRD) is employed to confirm the synthesis of hydroxyapatite, and scanning electron microscopy (SEM) is utilized to characterize morphology and elemental composition. At the bone organoid level, confocal fluorescence microscopy assesses the survival, growth, and spreading of internal cells. SEM is also used to observe the internal matrix structure and cell morphology of the bone organoids. Mineralization characteristics are primarily evaluated through micro-computed tomography (micro-CT) and transmission electron microscopy (TEM) to determine the degree of mineralization, calcium deposition, and crystallinity. Multicellular properties are validated through tissue section-specific staining. Functional evaluation is conducted using common markers such as OPN, OCN, and CD31 to assess osteogenesis and vascularization. Detailed experimental methods are provided in the **supplementary information**.

Reagents.

Gelatin (Aladdin, cat. no. L434330)
Sodium alginate (Aladdin, cat. no. A434496)
Hydroxyapatite (Aladdin, cat. no. H106378)
Methacrylate anhydride (Sigma-Aldrich, cat. no. 276685)
Calcium chloride ($CaCl_2$; Aladdin, cat. no. C598678)
Disodium hydrogen phosphate (NaH_2PO_4; Aladdin, cat. no. D433613)
Sodium hydroxide (NaOH; Aladdin, cat. no. S163080)
SD rats (Cavens; cat. no. C000121)
Anhydrous ethanol (Sigma-Aldrich, cat. no. E7023)
Phosphate Buffered Saline (PBS; Servicebio, cat. no. G4202)
Dulbecco's Modified Eagle Medium (DMEM; Thermo Scientific, cat. no. 11995065)
Type I collagenase (Sigma-Aldrich, cat. no. SCR103)
Fetal bovine serum (FBS; Sigma-Aldrich, cat. no. 12103C)
Penicillin-streptomycin (P/S; Sigma-Aldrich, cat. no. P4333)
Trypsin-EDTA (Thermo Scientific, cat. no. 25200072)
Lithium phenyl-2,4,6-trimethylbenzoylphosphinate (LAP; Aladdin, cat. no. L157759)
light absorber (EFL, cat. no. EFL-UVAW-001)
α-MEM (Thermo Scientific, cat. no. 12571063)
β-glycerophosphate (Aladdin, cat. no. D301908)
Ascorbic acid (Aladdin, cat. no. A103534)
Dexamethasone (Aladdin, cat. no. D137736)
BALB/c-Nude (Cavens; cat. no. C000103)
Isoflurane (Sigma-Aldrich, cat. no. 792632)

Equipment.

Magnetic stirrer (Lab Companion, model no. TS-14SG)
Sterile 50-ml centrifuge tube (NEST, cat. no. 602001)
Sterile 15-ml centrifuge tube (NEST, cat. no. 601001)
Freeze dryer (Labconoc, model no. FreeZone®)
70 μm cell strainer (NEST, cat. no. 258368)
Biosafety cabinet (Heal Force, model no. HFsafe-1200LC)
Centrifuge (Thermo Scientific SL8R, cat. no. 75007221)
Cell culture incubator (Panasonic, cat. no. MCO-19AICUV-PE)
100 mm culture dish (NEST, cat. no. 704004)
Light microscope (Nikon Eclipse, TS100)
Pipettes (Eppendorf Research, cat. no. 3123000039)
Pipettes (Eppendorf Research, cat. no. 3123000055)
Pipettes (Eppendorf Research, cat. no. 3123000268)
3D Studio Max software (Autodesk, USA)
Water bath pot (TATUNG, model no. WB-1-30)
Cell counter instrument (Countstar, model no. IC1000)
Cell counter slides (Countstar, cat. no. CO010101)
DLP printer manufactured in China (EFL-BP-8601 Pro)
0.22 μm filter (NEST, cat. no. 331011)
Plates, six-well (NEST, cat. no. 703001)
Isoflurane vaporizer (Mindray V60)
Anesthesia machine (EZ vet, model no. F700)
Sterile scalpel (RWD, China)
Sterile blunt forceps (RWD, China)
Sterile surgical thread (RWD, China)

5. Results

5.1. Characterization of bone-mimicking matrix hybrid hydroxyapatite bioink

The detailed characterization of the bone matrix-inspired hybrid hydroxyapatite bioink reveals its structural and compositional properties (Fig. 2). The NMR proton (^1H) spectrum confirms the successful grafting of methacrylate groups onto the bioink, as indicated by the characteristic chemical shifts around 6 ppm, which correspond to the vinyl protons ($CH_2 = CH-$) in the methacrylate structure. This region provides strong evidence for the presence of photopolymerizable groups. Additionally, peaks in the 1–2 ppm range likely represent alkyl chains, while those around 3–4 ppm may be associated with protons near oxygen atoms, such as in ester or hydroxyl groups. Overall, the spectrum reveals the successful modification of the bioink with methacrylate, enabling it to undergo light-curing (Fig. 2A). The XRD pattern confirms the successful synthesis of hydroxyapatite in the bioink, as indicated by the characteristic diffraction peaks corresponding to the (002), (211), (310), (222), and (213) planes, which align with the standard hydroxyapatite pattern from PDF#09–0432. The sharp and intense peak at the (211) plane, around $2\theta = 31.8^\circ$, is particularly notable, reflecting a well-formed crystalline structure. The overall peak sharpness and intensity suggest a high degree of crystallinity in the synthesized hydroxyapatite, verifying its successful integration into the bioink (Fig. 2B). The SEM image shows a loose porous structure, with a 3D network of interconnected pores observed. However, at this magnification, the inorganic hydroxyapatite phase is not directly visible, indirectly indicating that the hydroxyapatite exists in nanoscale form. The nanoparticle size of the hydroxyapatite makes it difficult to detect at the current resolution, allowing it to disperse well within the matrix without forming larger, detectable aggregates. This nanoscale incorporation enhances the bioactivity and mechanical integration of the material, supporting its application in bone tissue engineering (Fig. 2C). The state of the bioink undergoes significant changes before and after photopolymerization. Prior to photopolymerization, the hydrogel is in a liquid state, indicating its fluidity in the unpolymerized form, with the bioink components fully dissolved but not yet forming a solid structure. In contrast, after photopolymerization, the hydrogel successfully transitions into a solid gel, demonstrating that the photopolymerization process effectively converts the bioink solution into a stable hydrogel. This transformation confirms the efficacy of photopolymerization in the formation of a solid structure during bioink preparation (Fig. 2D). The energy-dispersive X-ray spectroscopy (EDS) analysis distinct peaks corresponding to key elements, including carbon (C), oxygen (O), phosphorus (P), and calcium (Ca). The presence of carbon and oxygen indicates the existence of organic components, which are typical of

biological materials. The peaks for phosphorus and calcium suggest the presence of mineralized structures, further confirming the existence of hydroxyapatite. The combination of C, O, P, and Ca elements provides further evidence of the coexistence of both organic (e.g., bioink components) and inorganic (e.g., bone-related minerals) materials within the sample, indicating the successful incorporation of bone-like minerals into the material structure. Additionally, no harmful or toxic elements were detected, with no peaks for heavy metals or other potentially hazardous substances. This result indirectly confirms the safety of the raw materials used in the synthesis process (Fig. 2E). The elemental mapping images illustrate the spatial distribution of these elements within the sample. The uniform distribution of each element indicates that these components are well-dispersed throughout the material (Fig. 2F).

5.2. Construction and bioactivity evaluation of bone organoids

Construction of bone organoids using advanced 3D bioprinting technology (Fig. 3). The schematic illustrates the 3D bioprinting process, highlighting the experimental steps of using DLP technology to print bone organoids from cell-laden bioink. Through DLP, the bioink undergoes layer-by-layer photopolymerization, precisely constructing the desired 3D structure and ultimately forming functional bone organoids (Fig. 3A). The 3D printing model created with 3D Max software is represented as a cylindrical structure with a regular matrix of holes. The matrix arrangement of these holes is designed to precisely control the distribution of printing materials, facilitate the exchange of nutrients, promote vascular ingrowth, and provide an optimized microenvironment for cell growth (Fig. 3B). The final product fabricated through 3D printing is highly consistent with the previously designed 3D model. The matrix arrangement of holes within the cylindrical structure is clearly visible and perfectly aligns with the geometric design of the model. This demonstrates that the bioink possesses excellent printability, maintaining design integrity during the printing process and successfully solidifying into the desired 3D structure (Fig. 3C). The live/dead cell staining (Calcein-AM/Propidium Iodide) results for the bone organoids, cultured *in vitro* for 7 days, show that green Calcium staining indicates most cells within the organoids are viable, with minimal red Propidium iodide (PI) staining (indicative of dead cells), further confirming the excellent biocompatibility and biosafety of the bioink. Additionally, the bright field images clearly reveal the structure, which aligns well with the designed organoid architecture. The microscopic images further support these findings, showing that the majority of the cells within the organoids are alive, with well-defined morphology and good cell spreading. These results suggest that the hydrogel not only supports cell viability but also promotes cell growth and functionality (Fig. 3D). High-resolution fluorescence images of bone organoids cultured *in vitro* for 7 days, using DAPI to stain nuclei and Rhodamine to label F-actin, further verify the cellular spreading within the constructs. In the DAPI-stained image, blue fluorescence clearly marks the location of the cell nuclei, indicating uniform cell distribution. The Rhodamine-labeled F-actin image shows red fluorescence highlighting the cytoskeleton, particularly the distribution of F-actin, confirming proper cell spreading and intercellular connections within the bone organoids. The merged image clearly illustrates the colocalization of nuclei and F-actin, further confirming the normal morphology and spreading of the cells (Fig. 3E).

5.3. Mineralization assessment of bone organoids

Evaluating the mineralization capability of bone organoids provides an in-depth understanding of their potential to form bone-like structures after implantation in a physiological environment (Fig. 4). This

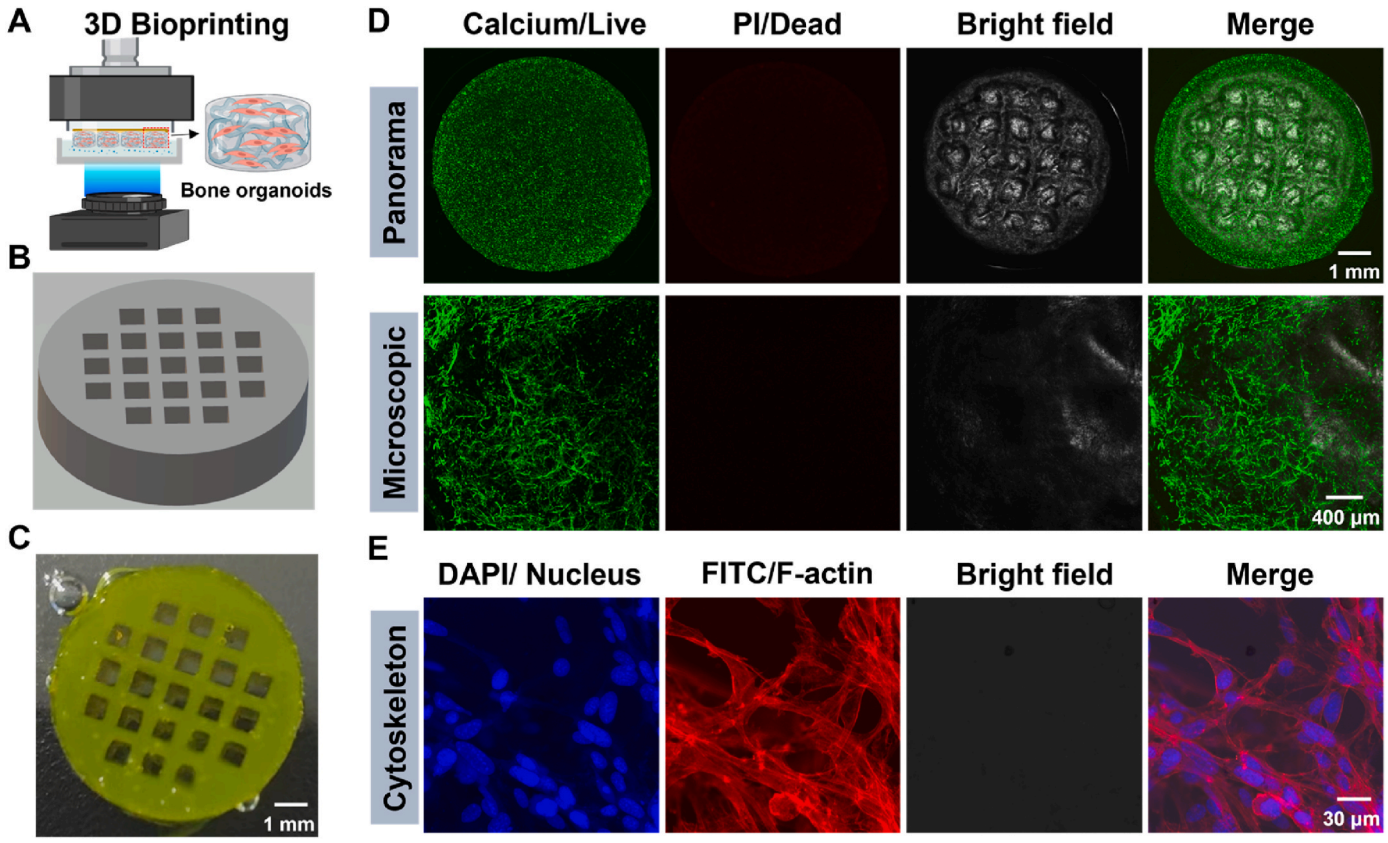

Fig. 3. 3D bioprinting and evaluation of bone organoids: structural integrity, cell viability, and morphological analysis. (A) Schematic of 3D bioprinting process. (B) 3D Max constructed model for 3D bioprinting. (C) Panoramic view of 3D printed bone organoids. (D) Cell viability and biocompatibility assessment of bone organoids. (E) High-resolution fluorescence imaging of the cytoskeleton in bone organoids.

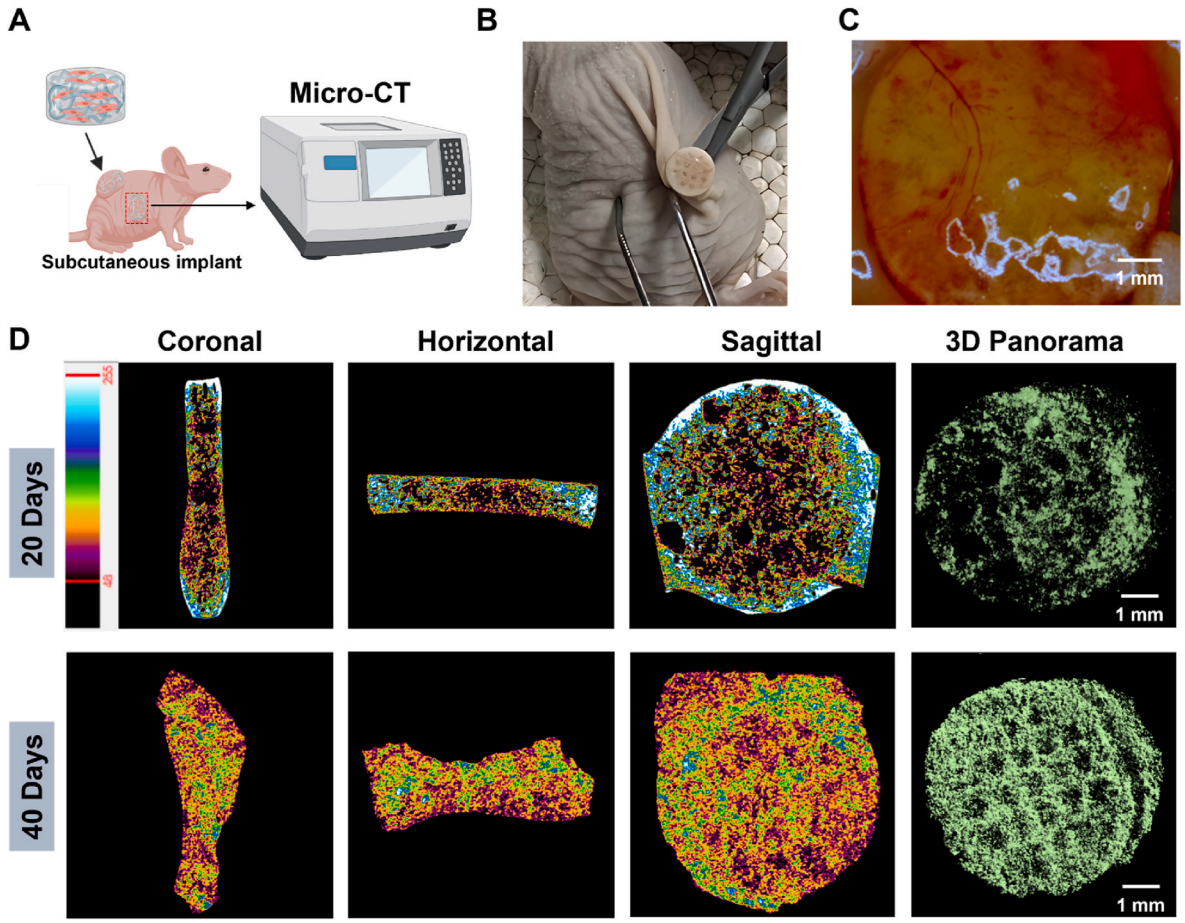

Fig. 4. *In vivo* mineralization evaluation of bone organoids. (A) Schematic of micro-CT scanning for bone organoids. (B) Surgical retrieval of bone organoids. (C) Stereomicroscopic analysis of vascularization in bone organoids. (D) *In vivo* mineralization progress of bone organoids assessed by micro-CT scanning.

assessment helps determine the effectiveness of bone organoids in mimicking the natural bone mineralization process. Micro-CT, as a non-invasive technique, enables longitudinal monitoring of mineralization without damaging the sample. Additionally, micro-CT provides high-resolution 3D imaging, allowing for detailed visualization of the mineralization process and the spatial distribution of mineral deposits within the bone organoids, facilitating a precise assessment of the quality and extent of mineralization. The schematic illustrates the experimental design for *in vivo* implantation and mineralization assessment of bone organoids. The bone organoids are implanted subcutaneously into nude mice, and after a period of cultivation, their mineralization performance is evaluated using micro-CT scanning. Micro-CT technology enables non-destructive evaluation of the degree of mineralization in the bone organoids and provides high-resolution 3D imaging, revealing the mineralization process and formation of bone-like structures in the *in vivo* environment (Fig. 4A). The surgical image shows the process of retrieving the bone organoid from the back of a nude mouse. Compared to before implantation, the bone organoid appears noticeably whiter, indicating that mineralization may have occurred during *in vivo* cultivation. Furthermore, the bone organoid maintained its overall shape without structural damage, demonstrating good stability in the *in vivo* environment. The color change is a typical sign of mineralization, usually caused by calcium deposition (Fig. 4B). Under stereomicroscopic observation, a clear vascular network was observed on the surface of the bone organoid, indicating successful induction of blood vessel formation and attachment to surrounding tissues. This vascularization suggests that the bone organoid has a strong ability to promote blood vessel formation after *in vivo* implantation. Vascularization is essential for the survival and functionality of large organoids, as it facilitates the efficient delivery of nutrients and oxygen, thereby supporting tissue growth and maturation (Fig. 4C). Micro-CT imaging shows the mineralization results of bone organoids after 20 and 40 days of *in vivo* cultivation in nude mice, evaluating the mineralization process through different sectional views (coronal, horizontal, sagittal) and 3D panoramic imaging. The color variations reflect differences in mineral density, with yellow representing high-density minerals and blue indicating lower-density cartilage tissue. After 20 days of cultivation, some regions begin to appear yellow, indicating initial mineralization, but there is still a considerable amount of low-density cartilage tissue (blue). After 40 days, the yellow regions increase significantly, suggesting a substantial enhancement in mineralization, demonstrating noticeable mineralization progress in bone organoids *in vivo*. Furthermore, 3D imaging displays the 3D structure of the mineralized areas, visually showing the distribution and extent of mineralization within the bone organoids, further confirming their mineralization process (Fig. 4D).

5.4. Multicellular morphology and spatial structure analysis of bone organoids

The internal cellular morphology and matrix structure of bone organoids, which were implanted subcutaneously into nude mice for 40 days, were analyzed in detail using biological SEM. SEM provided high-resolution imaging of the organoid's interior, revealing the morphological characteristics and arrangement of cells within the bone organoids. Additionally, the morphology of the extracellular matrix was observed (Fig. 5). The schematic illustrates the experimental design for SEM examination of bone organoids cultured *in vivo*. Bone organoids

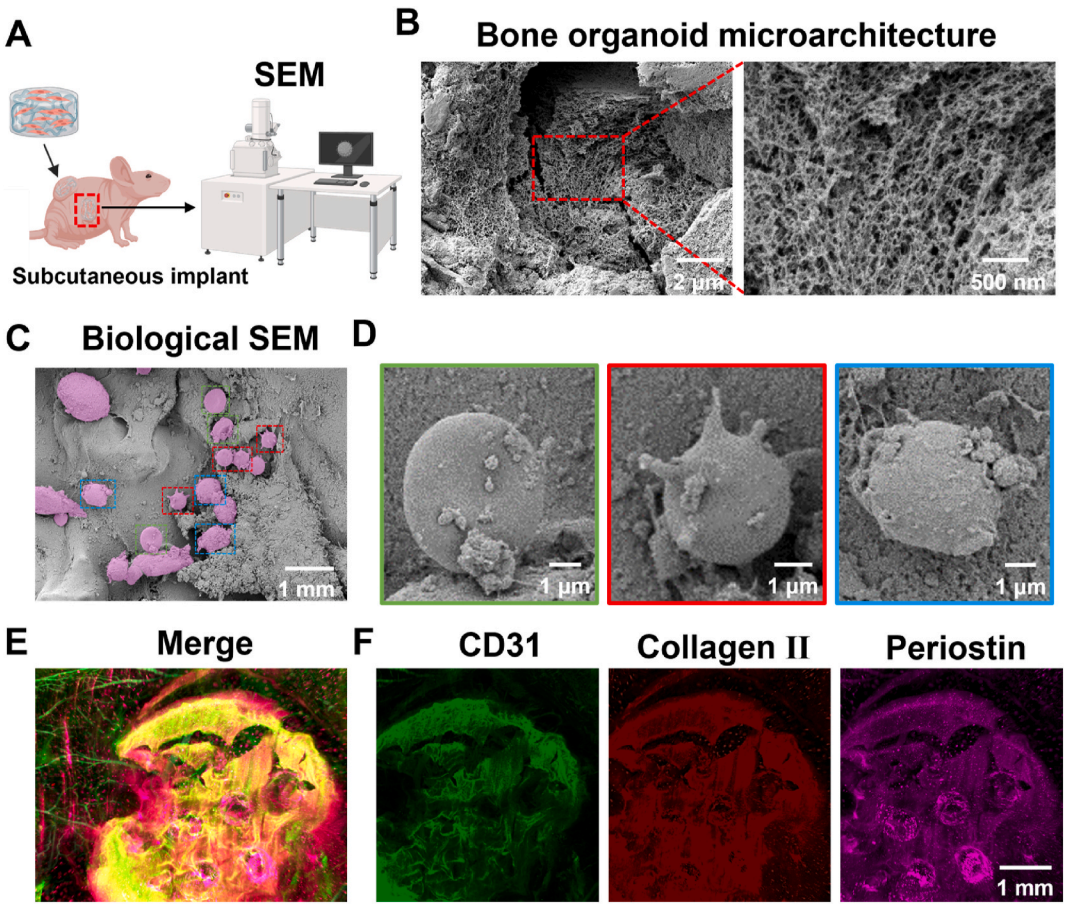

Fig. 5. Comprehensive morphological and structural analysis of bone organoids: SEM and 3D immunofluorescence imaging. (A) Experimental design for *in vivo* SEM evaluation of bone organoids. (B) Microarchitecture analysis of bone organoid via SEM scanning. (C) Cell morphological diversity of bone organoids via SEM scanning. (D) Identification of cell types in bone organoids via SEM scanning and morphological analysis. (E) 3D immunofluorescence analysis of specific markers in bone organoids. (F) Immunofluorescence analysis of CD31, collagen II, and periostin in bone organoids.

were implanted subcutaneously into a nude mouse, cultured *in vivo* for a period, then retrieved and evaluated using SEM high-resolution imaging to assess their internal cellular morphology and matrix structure (Fig. 5A). SEM imaging reveals the internal spatial structure of the bone organoid, clearly showing its loose and porous microarchitecture. Micron-level imaging displays the macroscopic cross-section of the bone organoid, while nanometer-level imaging provides detailed visualization of the complex pore network within. This structure closely resembles the characteristics of cancellous bone, indicating that the bone organoid possesses favorable bone-like structural properties (Fig. 5B). The regions marked with different colors highlight cells with diverse morphologies, including relatively rounded cells and some irregularly shaped cell clusters. The diversity in cell morphology indicates that bone organoids exhibit good cellular diversity and adaptability to the environment during *in vivo* cultivation (Fig. 5C). Although the exact identification of cell types cannot be definitively determined based solely on morphology, preliminary speculations can be made based on these observations. Through morphological comparison and analysis of previous literature [54,55], we classified these cells as red blood cells (RBCs), macrophages, and osteoblasts. RBCs exhibit a characteristic disc-like structure, macrophages display an active morphology with multiple protrusions, and osteoblasts show a more irregular surface structure. These observations suggest that vascular ingrowth into the bone organoid brought in myeloid-derived RBCs and macrophages, while BMSCs differentiated into osteoblasts, contributing to bone-like structure formation. These initial findings will be further verified through molecular biology experiments to confirm the specific types and functional states of the cells (Fig. 5D). Bone organoids underwent tissue clearing followed by 3D immunofluorescence imaging analysis. Fluorescent markers of different colors revealed the distribution of specific markers within the bone organoid: green fluorescence represents the vascular-specific marker CD31, red indicates the cartilage marker collagen II, and purple corresponds to the osteogenic-specific marker periostin. The merged image clearly shows the presence of distinct vascular lumens within the bone organoid, indicating successful induction of vascular formation and development during *in vivo* cultivation. Despite the presence of some non-specific staining, the vascular structures remain clearly visible. Additionally, the positive expression of collagen II and periostin further confirms the formation of cartilage and bone tissues within the bone organoid. These results demonstrate that the bone organoid possesses strong potential for vascularization, as well as osteogenic and chondrogenic differentiation (Fig. 5E–F).

5.5. *Crystallographic and elemental analysis of bone organoids*

The mechanical properties of bone organoids are closely related to the crystallization of hydroxyapatite within their structure. Hydroxyapatite is a crucial component that imparts rigidity and strength, mimicking the natural mineralized matrix found in bone. The degree of hydroxyapatite crystallization significantly affects the stiffness, compressive strength, and overall structural integrity of the bone organoids. In addition, elemental analysis provides insights into the chemical composition of the organoids, which should contain essential components similar to natural bone tissue to ensure proper biological function and mechanical performance (Fig. 6). Bone organoids were implanted subcutaneously into nude mice, cultured *in vivo* for 40 days, then

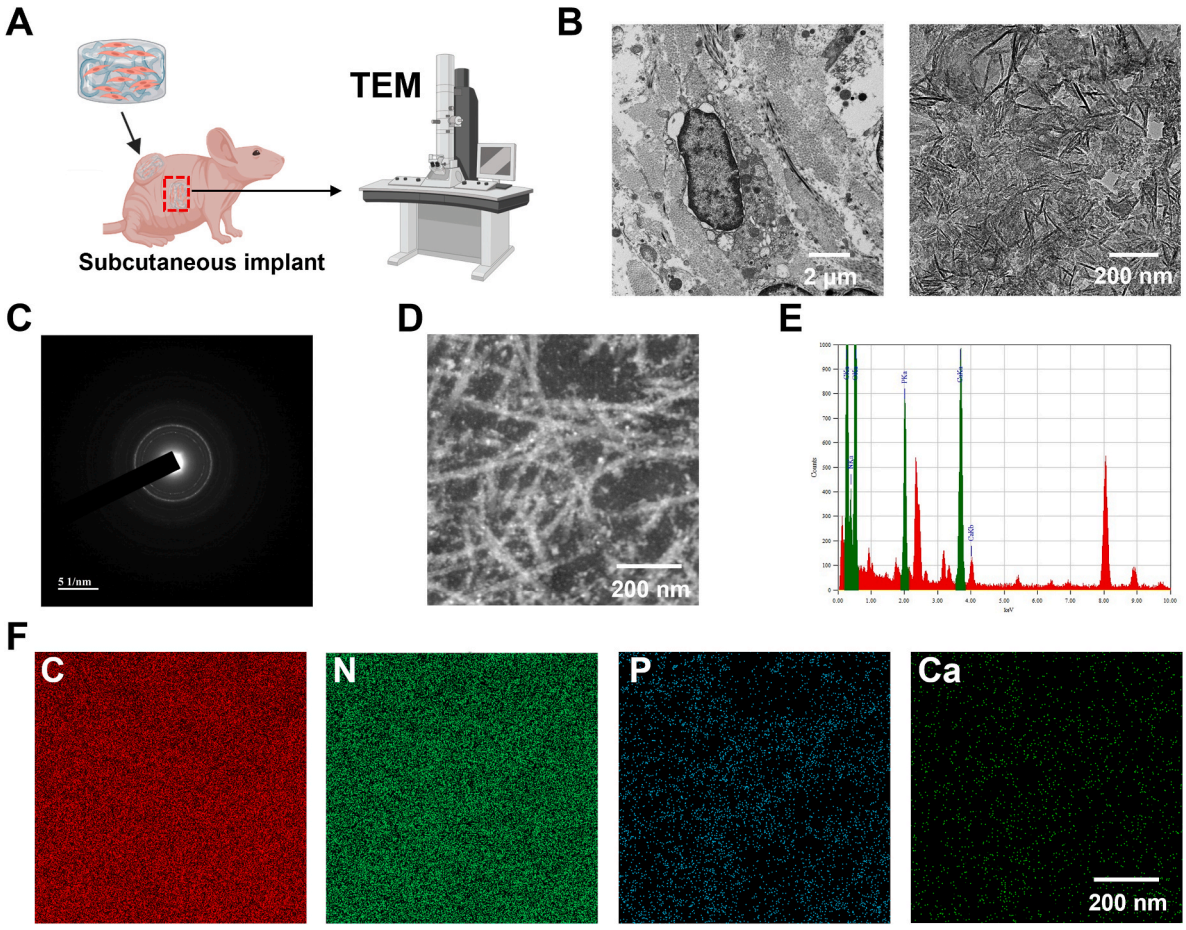

Fig. 6. Ultrastructural characterization and validation of mineralization crystals in bone organoids. (A) Experimental design for TEM examination of bone organoids. (B) Ultrastructural analysis of bone organoid mineralization using TEM scanning. (C) Electron diffraction analysis of crystalline mineral components in bone organoids. (D) Fibrous reticular structure of mineralized region in bone organoids. (E) Elemental composition analysis of bone organoids via EDS spectrum. (F) Elemental enrichment and distribution in bone organoids revealed by EDS mapping.

retrieved, sectioned, and prepared for scanning and observation using TEM (Fig. 6A). TEM images clearly reveal the ultrastructure of cells within the bone organoid, particularly highlighting the presence of cell nuclei, indicating well-preserved cellular morphology. Additionally, the images depict the nanocrystalline structure of the mineralized components within the bone organoid, suggesting that the mineral formation demonstrates good crystallinity, which is crucial for the mechanical properties and biological functions of bone-like tissue (Fig. 6B). The diffraction halo in the electron diffraction image further confirms that the mineralized components within the bone organoid have a crystalline structure. The presence of the halo indicates the existence of highly crystalline regions in the sample, consistent with the characteristics of mineral components such as hydroxyapatite, further supporting the successful mineralization process within bone organoids (Fig. 6C). The detailed analysis of the mineralized region within the bone organoid reveals a fibrous and reticular structure. EDS mapping was performed on this local area to further analyze its elemental composition and mineralization characteristics (Fig. 6D). The EDS spectrum reveals the elemental composition of the sample, clearly showing characteristic peaks for Ca and P, indicating significant enrichment of these elements within the sample. This enrichment of calcium and phosphorus further supports the formation of mineralized components within the bone organoid, particularly the presence of hydroxyapatite similar to that found in natural bone tissue (Fig. 6E). The elemental mapping images use different colors to represent specific elements: red for C, green for nitrogen (N), blue for P, and dark green for Ca. The uniform distribution of C and N indicates the presence of organic matrix, while the localized concentration of Ca and P further confirms the formation of mineralized components (Fig. 6F).

5.6. *Molecular biology identification of bone organoids*

The molecular biological identification of bone organoids primarily involves specific tissue staining to verify their bone-like structural characteristics, as well as immunofluorescence detection of bone tissue-related molecular markers (Fig. 7). After 40 days of subcutaneous implantation in nude mice, the bone organoids were retrieved and analyzed to confirm their development and characteristics. H&E staining results for the bone organoid demonstrate uniform tissue morphology and cell distribution. In an overall view, the internal structure of the organoid is homogeneous, maintaining a well-preserved form, while the magnified view reveals the distribution of cells within the matrix, showing clear boundaries between the cells and the extracellular matrix. This findings indicates effective cell viability and distribution within the 3D environment. These results indicate that the bone organoid has a stable internal structure, making it suitable for further investigation of cellular and tissue functions (Fig. 7A). Masson staining results illustrate the distribution of collagen fibers and cells within the bone organoid. In the overall view, blue staining clearly indicates the presence of a rich collagen fiber network throughout the organoid, while the red areas mainly highlight cellular components and other proteins within the matrix. The magnified view further reveals detailed collagen fiber distribution and their relationship with the cells. The red fibers are distinctly visible, interwoven with the blue matrix,

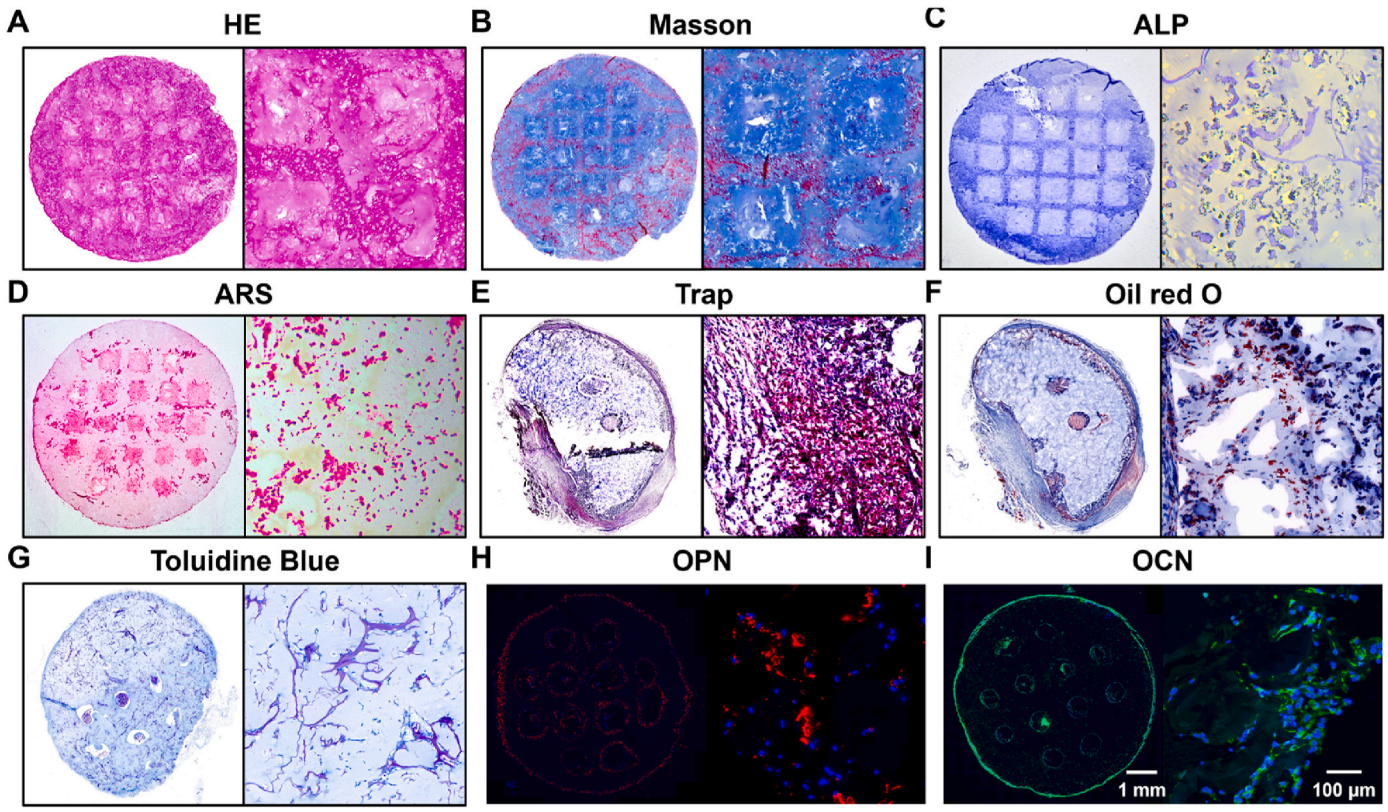

Fig. 7. Histological staining of bone organoids. (A) HE staining of bone organoids. (B) Masson's Trichrome staining of bone organoids. (C) ALP staining of bone organoids. (D) ARS staining of bone organoids. (E) TRAP staining of bone organoids. (F) Oil Red O staining of bone organoids. (G) Toluidine blue staining of bone organoids. (H) Immunofluorescence staining of OPN in bone organoids. (I) Immunofluorescence staining of OCN in bone organoids.

demonstrating a well-organized tissue structure and effective integration between cells and the matrix (Fig. 7B). The results of alkaline phosphatase (ALP) and alizarin red S (ARS) staining demonstrate the osteogenic activity and mineralization of the bone organoids. ALP staining was used to detect alkaline phosphatase activity, an important marker of osteoblast differentiation. In the overall view, significant blue staining can be observed within the organoid, indicating the presence of active osteoblasts. The magnified image further reveals the distribution of ALP activity. ARS staining was used to detect mineralized nodules, with distinct red staining observed both in the overall and magnified images, indicating the formation of mineralized nodules during *in vivo* culture, thereby confirming effective mineralization in the bone organoids (Fig. 7C–D). Tartrate-resistant acid phosphatase (TRAP) staining was used to detect osteoclast activity within the bone organoid. In the overall TRAP staining view, the bone organoid exhibited purple-red staining regions, indicating high osteoclast activity in these areas. The magnified view further clearly shows the distribution of osteoclasts, with purple-red regions representing areas enriched with osteoclasts. These findings demonstrate the presence of active osteoclasts within the bone organoid, which is significant for modeling the remodeling process of bone tissue (Fig. 7E). The Oil Red O staining results indicate the presence of lipid accumulation within the bone organoid. In the overall view, the red-stained regions clearly show the distribution of lipids, while the magnified image further reveals the details of the lipid droplets. The red-marked areas distinctly demonstrate the presence of adipocytes in the bone organoid, suggesting its potential for adipogenesis during *in vivo* cultivation (Fig. 7F). The toluidine blue staining results revealed the matrix structure and cellular components within the bone organoid, particularly highlighting the presence of chondrocytes. In the overall view, the blue-stained areas demonstrated the distribution of the extracellular matrix, while the magnified images further illustrated the details of chondrocytes and collagen fibers within the matrix. These staining results indicate that the bone organoid contains matrix components and chondrocyte arrangement similar to those found in the endochondral ossification process (Fig. 7G). OPN, a multifunctional protein involved in both early bone formation and mineralization, is prominently expressed. OPN mediates cell-matrix interactions, promotes mineral deposition, and regulates the remodeling of bone tissue. The detection of OPN fluorescence underscores the active mineralization occurring within the bone organoids, which is essential for developing a functional bone matrix that mimics native bone tissue properties (Fig. 7H). In addition to OPN, the expression of OCN, a well-established marker of late-stage osteogenesis, is also observed. This strong fluorescence signal for OCN indicates the presence of mature osteoblasts actively contributing to bone matrix deposition, signifying that the bone organoids have successfully progressed beyond the early differentiation stages to achieve a more advanced, mature bone-like state (Fig. 7I).

In summary, the experimental results provide strong evidence that bone organoids successfully recapitulate key aspects of bone development, making them a valuable model for studying bone biology and potentially applicable in fields such as bone regeneration, disease modeling, and drug screening. The ability to visualize and confirm these key markers through immunofluorescence provides important insights into the dynamic cellular and molecular mechanisms of osteogenesis in 3D organoid models.

6. Limitations

Despite significant advancements, several limitations must be addressed to enhance the broader application and development of bone organoids. One major challenge is replicating the complex physiological environment of bone tissue, including intricate interactions among bone, bone marrow, and immune cells. Many current bone organoid models lack adequate vascularization, which is crucial for nutrient

delivery and waste removal, limiting their ability to mimic *in vivo* conditions accurately. Additionally, bone organoids remain simplified and do not fully capture the dynamic interactions between bone, cartilage, and surrounding tissues. Our study employs rat BMSCs to construct bone organoids, but interspecies differences between rat and human MSCs—including variations in differentiation potential, proliferation rates, and immune responses—may affect the translational applicability of these findings. Therefore, further validation using human MSCs is necessary to confirm the clinical relevance of our results. Furthermore, scaling up current protocols for high-throughput applications remains challenging due to labor-intensive processes that are difficult to standardize. Mechanical loading, a key factor in bone remodeling, is not yet fully integrated into existing models, and maintaining the long-term stability of bone organoids under conditions that simulate aging or chronic diseases remains a significant hurdle. Addressing these challenges will require integrating advanced bioengineering techniques and more sophisticated models to create physiologically relevant, scalable, and stable bone organoid systems that can reliably mimic the complexity of bone tissue *in vivo*.

CRediT authorship contribution statement

Jian Wang: Writing – original draft, Methodology, Investigation, Formal analysis, Data curation, Conceptualization. **Dongyang Zhou:** Methodology, Investigation. **Ruiyang Li:** Methodology, Investigation, Formal analysis. **Shihao Sheng:** Writing – review & editing, Investigation, Formal analysis. **Guangfeng Li:** Validation, Formal analysis. **Yue Sun:** Validation, Supervision, Conceptualization. **Peng Wang:** Methodology. **Yulin Mo:** Methodology. **Han Liu:** Validation, Supervision, Conceptualization. **Xiao Chen:** Writing – review & editing, Methodology, Conceptualization. **Zhen Geng:** Methodology. **Qin Zhang:** Methodology, Conceptualization. **Yingying Jing:** Writing – review & editing, Supervision, Resources. **Long Bai:** Writing – review & editing, Supervision, Resources. **Ke Xu:** Writing – review & editing, Supervision, Resources. **Jiacan Su:** Writing – review & editing, Supervision, Resources, Project administration, Funding acquisition, Conceptualization.

Ethics approval and consent to participate

All animal experimental procedures were strictly conducted in accordance with the established guidelines for animal experiments and had received approval from the Animal Ethics Committee of Shanghai University (ECSHU 2022–088).

Declaration of competing interest

The authors declare that they have no known competing financial interests or personal relationships that could have appeared to influence the work reported in this paper.

Acknowledgement

The authors acknowledge the financial support from National Natural Science Foundation of China (82230071, 82172098, 82472444), Shanghai Committee of Science and Technology (23141900600, Laboratory Animal Research Project), Shanghai Clinical Research Plan of SHDC2023CRT01, and Generaral Project of Natural Science Foundation of Jiangsu Province (BK20231218). The authors would like to thank Servicebio Technology Co., Ltd. for their technical support and provision of reagents used in bone organoid tissue sectioning and staining.

Appendix A. Supplementary data

Supplementary data to this article can be found online at https://doi.org/10.1016/j.bioactmat.2024.11.017.

References

[1] J. Wang, X. Li, S. Wang, J. Cui, X. Ren, J. Su, Bone-targeted exosomes: strategies and applications, Adv. Healthcare Mater. 12 (18) (2023) 2203361.
[2] A.T. Nguyen, I.M. Aris, B.D. Snyder, M.B. Harris, J.D. Kang, M. Murray, E. K. Rodriguez, A. Nazarian, Musculoskeletal health: an ecological study assessing disease burden and research funding, The Lancet Regional Health – Americas 29 (2024).
[3] D. Lopes, C. Martins-Cruz, M.B. Oliveira, J.F. Mano, Bone physiology as inspiration for tissue regenerative therapies, Biomaterials 185 (2018) 240–275.
[4] R. Florencio-Silva, G.R.d.S. Sasso, E. Sasso-Cerri, M.J. Simões, P.S. Cerri, Biology of bone tissue: structure, function, and factors that influence bone cells, BioMed Res. Int. 2015 (1) (2015) 421746.
[5] L.J. Raggatt, N.C. Partridge, Cellular and molecular mechanisms of bone remodeling, J. Biol. Chem. 285 (33) (2010) 25103–25108.
[6] S. Amin, Mechanical factors and bone health: effects of weightlessness and neurologic injury, Curr. Rheumatol. Rep. 12 (3) (2010) 170–176.
[7] M. Maryanovich, S. Takeishi, P.S. Frenette, Neural regulation of bone and bone marrow, Cold Spring Harb Perspect Med 8 (9) (2018).
[8] E.C. Watson, R.H. Adams, Biology of bone: the vasculature of the skeletal system, Cold Spring Harb Perspect Med 8 (7) (2018).
[9] R. Dimitriou, E. Jones, D. McGonagle, P.V. Giannoudis, Bone regeneration: current concepts and future directions, BMC Med. 9 (1) (2011) 66.
[10] G. Chindamo, S. Sapino, E. Peira, D. Chirio, M.C. Gonzalez, M. Gallarate, Bone diseases: current approach and future perspectives in drug delivery systems for bone targeted therapeutics, Nanomaterials 10 (5) (2020) 875.
[11] L.H. Goetz, N.J. Schork, Personalized medicine: motivation, challenges, and progress, Fertil. Steril. 109 (6) (2018) 952–963.
[12] A. Rodríguez Ruiz, M. van Hoolwerff, S. Sprangers, E. Suchiman, T. Schoenmaker, P. Dibbets-Schneider, J.L. Bloem, R. Nelissen, C. Freund, C. Mummery, V. Everts, T. J. de Vries, Y.F.M. Ramos, I. Meulenbelt, Mutation in the CCAL1 locus accounts for bidirectional process of human subchondral bone turnover and cartilage mineralization, Rheumatology 62 (1) (2022) 360–372.
[13] S. Choudhary, P. Ramasundaram, E. Dziopa, C. Mannion, Y. Kissin, L. Tricoli, C. Albanese, W. Lee, J. Zilberberg, Human ex vivo 3D bone model recapitulates osteocyte response to metastatic prostate cancer, Sci. Rep. 8 (1) (2018) 17975.
[14] D. Zhao, Q. Saiding, Y. Li, Y. Tang, W. Cui, Bone organoids: recent advances and future challenges, Adv. Healthcare Mater. 13 (5) (2024) 2302088.
[15] J. Huang, L. Zhang, A. Lu, C. Liang, Organoids as innovative models for bone and joint diseases, Cells 12 (12) (2023) 1590.
[16] S. Chen, X. Chen, Z. Geng, J. Su, The horizon of bone organoid: a perspective on construction and application, Bioact. Mater. 18 (2022) 15–25.
[17] Y. Park, E. Cheong, J.-G. Kwak, R. Carpenter, J.-H. Shim, J. Lee, Trabecular bone organoid model for studying the regulation of localized bone remodeling, Sci. Adv. 7 (4) (2021) eabd6495.
[18] D.M. Abraham, C. Herman, L. Witek, B.N. Cronstein, R.L. Flores, P.G. Coelho, Self-assembling human skeletal organoids for disease modeling and drug testing, J. Biomed. Mater. Res. B Appl. Biomater. 110 (4) (2022) 871–884.
[19] G. Nilsson Hall, L.F. Mendes, C. Gklava, L. Geris, F.P. Luyten, I. Papantoniou, Developmentally engineered callus organoid bioassemblies exhibit predictive in vivo long bone healing, Adv. Sci. 7 (2) (2020) 1902295.
[20] A.O. Khan, A. Rodriguez-Romera, J.S. Reyat, A.-A. Olijnik, M. Colombo, G. Wang, W.X. Wen, N. Sousos, L.C. Murphy, B. Grygielska, G. Perrella, C.B. Mahony, R. E. Ling, N.E. Elliott, C.S. Karali, A.P. Stone, S. Kemble, E.A. Cutler, A.K. Fielding, A. P. Croft, D. Bassett, G. Poologasundarampillai, A. Roy, S. Gooding, J. Rayes, K. R. Machlus, B. Psaila, Human bone marrow organoids for disease modeling, discovery, and validation of therapeutic targets in hematologic malignancies, Cancer Discov. 13 (2) (2023) 364–385.
[21] J. Wu, Z. Yang, B. Yang, H. Huang, The application of organoids in the research of skeletal diseases: current status and prospects, Stud. Health Technol. Inf. 308 (2023) 597–604.
[22] L. Bai, D. Zhou, G. Li, J. Liu, X. Chen, J. Su, Engineering bone/cartilage organoids: strategy, progress, and application, Bone Res. 12 (1) (2024) 66.
[23] J. Fuller, K. Lefferts, P. Shah, J. Cottrell, Methodology and characterization of a 3D bone organoid model derived from murine cells, Int. J. Mol. Sci. 25 (2024) 4225.
[24] K. Dai, Q. Zhang, S. Deng, Y. Yu, F. Zhu, S. Zhang, Y. Pan, D. Long, J. Wang, C. Liu, A BMP-2–triggered in vivo osteo-organoid for cell therapy, Sci. Adv. 9 (1) (2023) eadd1541.
[25] H. Liu, X. Zhang, J. Liu, J. Qin, Vascularization of engineered organoids, BMEMat 1 (3) (2023) e12031.
[26] F. Liu, Q. Wu, Q. Liu, B. Chen, X. Liu, J.L. Pathak, N. Watanabe, J. Li, Dental pulp stem cells-derived cannabidiol-treated organoid-like microspheroids show robust osteogenic potential via upregulation of WNT6, Commun. Biol. 7 (1) (2024) 972.
[27] A.-A. Olijnik, A. Rodriguez-Romera, Z.C. Wong, Y. Shen, J.S. Reyat, N.J. Jooss, J. Rayes, B. Psaila, A.O. Khan, Generating human bone marrow organoids for disease modeling and drug discovery, Nat. Protoc. 19 (7) (2024) 2117–2146.
[28] Z. Yang, B. Wang, W. Liu, X. Li, K. Liang, Z. Fan, J.J. Li, Y. Niu, Z. He, H. Li, D. Wang, J. Lin, Y. Du, J. Lin, D. Xing, In situ self-assembled organoid for osteochondral tissue regeneration with dual functional units, Bioact. Mater. 27 (2023) 200–215.
[29] J. Qing, Q. Guo, L. Lv, X. Zhang, Y. Liu, B.C. Heng, Z. Li, P. Zhang, Y. Zhou, Organoid culture development for skeletal systems, Tissue Eng., Part B 29 (5) (2023) 545–557.
[30] J. Zhang, J. Griesbach, M. Ganeyev, A.K. Zehnder, P. Zeng, G.N. Schädli, A. Leeuw, Y. Lai, M. Rubert, R. Müller, Long-term mechanical loading is required for the

formation of 3D bioprinted functional osteocyte bone organoids, Biofabrication 14 (3) (2022).
[31] J. Wang, Y. Wu, G. Li, F. Zhou, X. Wu, M. Wang, X. Liu, H. Tang, L. Bai, Z. Geng, P. Song, Z. Shi, X. Ren, J. Su, Engineering large-scale self-mineralizing bone organoids with bone matrix-inspired hydroxyapatite hybrid bioinks, Adv. Mater. 36 (30) (2024) 2309875.
[32] X. Ren, J. Wang, Y. Wu, Y. Zhang, J. Zhang, L. Bai, J. Liu, G. Li, P. Song, Z. Shi, J. Su, One-pot synthesis of hydroxyapatite hybrid bioinks for digital light processing 3D printing in bone regeneration, J. Mater. Sci. Technol. 188 (2024) 84–97.
[33] C. Pleguezuelos-Manzano, J. Puschhof, S. van den Brink, V. Geurts, J. Beumer, H. Clevers, Establishment and culture of human intestinal organoids derived from adult stem cells, Curr. Protoc. Im. 130 (1) (2020) e106.
[34] A.J. Miller, B.R. Dye, D. Ferrer-Torres, D.R. Hill, A.W. Overeem, L.D. Shea, J. R. Spence, Generation of lung organoids from human pluripotent stem cells in vitro, Nat. Protoc. 14 (2) (2019) 518–540.
[35] D. Hendriks, B. Artegiani, H. Hu, S. Chuva de Sousa Lopes, H. Clevers, Establishment of human fetal hepatocyte organoids and CRISPR–Cas9-based gene knockin and knockout in organoid cultures from human liver, Nat. Protoc. 16 (1) (2021) 182–217.
[36] R. Morizane, J.V. Bonventre, Generation of nephron progenitor cells and kidney organoids from human pluripotent stem cells, Nat. Protoc. 12 (1) (2017) 195–207.
[37] F. Wang, P. Song, J. Wang, S. Wang, Y. Liu, L. Bai, J. Su, Organoid bioinks: construction and application, Biofabrication 16 (3) (2024) 032006.
[38] Y. Gao, N. Chen, Z. Fu, Q. Zhang, Progress of wnt signaling pathway in osteoporosis, Biomolecules 13 (3) (2023).
[39] S. Zhu, W. Chen, A. Masson, Y.-P. Li, Cell signaling and transcriptional regulation of osteoblast lineage commitment, differentiation, bone formation, and homeostasis, Cell Discovery 10 (1) (2024) 71.
[40] C. Li, Y. Zhang, Y. Du, Z. Hou, Y. Zhang, W. Cui, W. Chen, A review of advanced biomaterials and cells for the production of bone organoid, Small Science 3 (8) (2023) 2300027.
[41] C. Xie, R. Liang, J. Ye, Z. Peng, H. Sun, Q. Zhu, X. Shen, Y. Hong, H. Wu, W. Sun, X. Yao, J. Li, S. Zhang, X. Zhang, H. Ouyang, High-efficient engineering of osteo-callus organoids for rapid bone regeneration within one month, Biomaterials 288 (2022) 121741.
[42] D. Janagama, S.K. Hui, 3-D cell culture systems in bone marrow tissue and organoid engineering, and BM phantoms as in vitro models of hematological cancer therapeutics—a review, Materials 13 (24) (2020) 5609.
[43] Y. Kong, Y. Yang, Y. Hou, Y. Wang, W. Li, Y. Song, Advance in the application of organoids in bone diseases, Front. Cell Dev. Biol. 12 (2024).
[44] A. Pievani, B. Sacchetti, A. Corsi, B. Rambaldi, S. Donsante, V. Scagliotti, P. Vergani, C. Remoli, A. Biondi, P.G. Robey, M. Riminucci, M. Serafini, Human umbilical cord blood-borne fibroblasts contain marrow niche precursors that form a bone/marrow organoid in vivo, Development 144 (6) (2017) 1035–1044.
[45] X. Zhao, N. Li, Z. Zhang, J. Hong, X. Zhang, Y. Hao, J. Wang, Q. Xie, Y. Zhang, H. Li, M. Liu, P. Zhang, X. Ren, X. Wang, Beyond hype: unveiling the Real challenges in clinical translation of 3D printed bone scaffolds and the fresh prospects of bioprinted organoids, J. Nanobiotechnol. 22 (1) (2024) 500.
[46] M. Mirshafiei, H. Rashedi, F. Yazdian, A. Rahdar, F. Baino, Advancements in tissue and organ 3D bioprinting: current techniques, applications, and future perspectives, Mater. Des. 240 (2024) 112853.
[47] J.E. Cardier, D. Diaz-Solano, O. Wittig, G. Sierra, J. Pulido, R. Moreno, S. Fuentes, F. Leal, Osteogenic organoid for bone regeneration: healing of bone defect in congenital pseudoarthrosis of the tibia, Int. J. Artif. Organs 47 (2) (2024) 107–114.
[48] V. Blay, B. Tolani, S.P. Ho, M.R. Arkin, High-throughput screening: today's biochemical and cell-based approaches, Drug Discov. Today 25 (10) (2020) 1807–1821.
[49] W.L. Tam, L. Freitas Mendes, X. Chen, R. Lesage, I. Van Hoven, E. Leysen, G. Kerckhofs, K. Bosmans, Y.C. Chai, A. Yamashita, N. Tsumaki, L. Geris, S. J. Roberts, F.P. Luyten, Human pluripotent stem cell-derived cartilaginous organoids promote scaffold-free healing of critical size long bone defects, Stem Cell Res. Ther. 12 (1) (2021) 513.
[50] B. Long, L. Mengmeng, S. Jiacan, 432A perspective on light-based bioprinting of DNA hydrogels for advanced bone regeneration: implication for bone organoids, Int J Bioprint 9 (2) (2023) 688.
[51] A. Sarachakov, A. Varlamova, V. Svekolkin, M. Polyakova, I. Valencia, C. Unkenholz, T. Pannellini, I. Galkin, P. Ovcharov, D. Tabakov, E. Postovalova, N. Shin, I. Sethi, A. Bagaev, T. Itkin, G. Crane, M. Kluk, J. Geyer, G. Inghirami, S. Patel, Spatial mapping of human hematopoiesis at single-cell resolution reveals aging-associated topographic remodeling, Blood 142 (26) (2023) 2282–2295.
[52] M.H. Geurts, H. Clevers, CRISPR engineering in organoids for gene repair and disease modelling, Nature Reviews Bioengineering 1 (1) (2023) 32–45.
[53] L. Bai, J. Li, G. Li, D. Zhou, J. Su, C. Liu, Skeletal interoception and prospective application in biomaterials for bone regeneration, Bone Research (2024).
[54] J. Bain, N.A.R. Gow, L.-P. Erwig, Novel insights into host-fungal pathogen interactions derived from live-cell imaging, Semin. Immunopathol. 37 (2) (2015) 131–139.
[55] U.E. Pazzaglia, T. Congiu, V. Sibilia, D. Quacci, Osteoblast-osteocyte transformation. A SEM densitometric analysis of endosteal apposition in rabbit femur, J. Anat. 224 (2) (2014) 132–141.